The Spherically Symmetric Collapse of Collisionless Matter

Exploring Critical Phenomena through Finite Volume Methods

by

Roland Stevenson

B.Sc., Acadia University, 2003

A THESIS SUBMITTED IN PARTIAL FULFILMENT OF
THE REQUIREMENTS FOR THE DEGREE OF

Master of Science

in

The Faculty of Graduate Studies

(Physics)

The University Of British Columbia

November 10, 2005

In presenting this thesis in partial fulfilment of the requirements for an advanced degree at the University of British Columbia, I agree that the Library shall make it freely available for reference and study. I further agree that permission for extensive copying of this thesis for scholarly purposes may be granted by the head of my department or by his or her representatives. It is understood that copying or publication of this thesis for financial gain shall not be allowed without my written permission.

(Signature) _____

Department of Physics and Astronomy

The University Of British Columbia
Vancouver, Canada

Date _____

ABSTRACT

We present a novel numerical study of critical phenomena in the massive, spherically symmetric Einstein-Vlasov system. After casting of the Vlasov equation in flux-conservative form, a finite volume approach is used to evolve the distribution function in phase space. Such an approach yields solutions with well defined convergence behavior; a property both crucial for critical phenomena research and also one that supersedes previous Monte-Carlo dominated Einstein-Vlasov research. Up to machine precision, and in accord with work by Schaeffer, Rein and Rendall [12] and Olabarietta and Choptuik [19, 20], the critical solution for distributions having constant angular-momentum-squared-per-particle, l^2, are shown to be static intermediate attractors. Near-critical solutions are also shown to exhibit the logarithmic scaling associated with Type I critical phenomena.

We also look at critical phenomena for two interacting distributions with different values of l^2, displaying evidence that even in this two-species coupled case, the critical solution exhibits Type I scaling and staticity.

Finally, the massless case is studied, and evidence for Type I scaling and staticity is presented.

The question of whether or not the critical solution is universal remains unanswered for all cases. However, at least without some nontrivial rescaling of variables, there is no clear evidence for universality in our results at the current time.

CONTENTS

LIST OF TABLES

LIST OF FIGURES

ACKNOWLEDGEMENTS

For my parents, Helga and Lloyd Stevenson.

PART I

Thesis

CHAPTER 1

INTRODUCTION

Critical phenomena describe the behavior of solutions to Einstein's equations coupled to matter at the threshold of black hole formation (see Gundlach [14] for a comprehensive recent review of this subject). Given an initial configuration of matter described by one parameter, p, as it evolves, the configuration will either collapse (supercritical evolution) or disperse (subcritical evolution). In practice one is limited by the precision of a computer in constructing a critical solution exactly on the boundary between dispersal and collapse. Therefore, numerically, one typically "tunes" p until it approximates the critical parameter $p^\star$, to machine precision (and for some specific discretization parameters, such as the basic mesh scale, h).

Type I critical phenomena exhibit three distinguishing characteristics as p approaches $p^\star$: they describe static, though unstable, spacetimes; nearly critical solutions have lifetimes that scale logarithmically with $|p - p^\star|$; critical solutions are posited to be universal, in that different initial conditions—for a fixed model—produce the same critical behavior. These characteristics, and critical phenomena *per se*, were first discovered by Choptuik [4].

This thesis provides evidence for two of the above three characteristics for the massive spherically symmetric Einstein-Vlasov system, namely staticity and scaling. Chapter 2 reviews the governing equations of the system. Chapter 3 describes how to write the evolution equation in flux conservative form as well as the novel numerical techniques underlying finite volume methods for flux-

conservative equations. Chapter 4 shows in detail that the code converges and that as it converges, so does conservation of mass (as consistency demands!). Finally, Chapter 5 provides numerical evidence for the existence of Type I critical phenomena in various Einstein-Vlasov systems.

1.1   A Brief History of Critical Phenomena

Critical phenomena trace their roots back to a discussion between Christodoulou and Chopuik [9, 10] in 1987. While studying scalar field collapse from a closed-form (often called "analytical") standpoint, Christodoulou posed the following question to Choptuik, who was studying the same system numerically: "At the threshold of black hole formation, does a scalar field form a finite-mass black hole, or an infinitesimally-small black hole?" Choptuik set to work developing advanced numerical techniques in order to answer this question, and in his response the field of critical phenomena in gravitational collapse was born [4].

Following the discovery of critical phenomena in the gravitational collapse of a scalar field, critical phenomena were discovered in other systems including SU(2) Yang-Mills fields[16], fluids [21, 3, 11], and non-linear sigma models [23], as well as in axi-symmetric collapse scenarios [18] [17].

Critical solutions in any system of equations are found by defining a parameter p in the model, which, when varied, produces either dispersive or collapse behavior in the model. These two end states of the model represent a bifurcation, and the p which lies exactly on the boundary between the two choices, called $p^\star$, defines what is known as the critical solution. It represents the solution which is closest to forming a black hole, but will nonetheless *not* form a black hole. The phenomena associated with this particular solution are, not surprisingly, known as critical phenomena.

In analogy with statistical mechanics, critical phenomena can be of Type

I or II. Type II critical phenomena, discovered first, allow for a continuous phase transition during the onset of a black hole, where the black hole mass represents the order parameter. In other words, the black holes formed can have infinitesimal mass. In Type I phenomena, on the other hand, infinitesimal black holes cannot be created, and the black hole "turns on" at finite mass. Thus, the closest solution (on the collapse side) to the critical solution contains a finite-mass black hole.

Type I critical phenomena are known to have scaling relationships of the following form:

$$|t - t^\star| = \ln |p - p^\star|^\sigma \qquad (1.1)$$

Here, t represents the time a solution defined by parameter p spends within the critical regime—an arbitrarily defined radius for all examples contained within this thesis. Clearly, (1.1) shows that the time spent near the critical solution increases logarithmically with how close the solution is to criticality in parameter space. Furthermore, the scaling exponent, σ, is conjectured to be universal for all sets of initial data, and for *fixed physical model*. Note that specification of the model can involve other tunable parameters, such as our angular momentum parameter, l^2, below, and that we do *not* necessarily expect to see true unversality as all possible model parameters are varied. Finally, Type I critical solutions are conjectured to be either static or periodic, whereas Type II critical phenomena exhibit scale symmetry (self-similarity), also in both continuous and discrete varieties. Again, the reader interested in additional details is referred to the excellent review by Gundlach [14]

This thesis considers the critical regime of spherically symmetric clouds of collisionless matter. Scaling relationships of the form (1.1) are observed and tabulated for a variety of initial conditions. Finally, the approximately critical solutions are shown to resemble static (Type I) solutions.

1.2   Collisionless Matter

Collisionless matter represents one of many possible "toy models" for a self-gravitating system. As one might guess, collisionless matter only interacts through its gravitational field, and therefore contains no inherent pressure. Every particle of collisionless matter in spherical symmetry can have a particular position and radial momentum, and therefore naturally "lives" in a two dimensional phase space—one dimension representing the radial location of the shell, the other representing the shell's radial momentum. It is this two dimensional phase space that we choose to exploit in modelling the dynamics of critical phenomena.

If we consider a spherical shell of collisionless matter, without any repulsive central potential it will naturally collapse inwards on itself in all cases. We include an angular momentum term in the equations, which provides an effective repulsive central potential which the ingoing spherical shell "feels" as it collapses on itself. Thus, the angular momentum provides the repulsive self-interaction in the model that is needed to "balance" the attractive gravitational self-interaction and create a critical solution.

One may ask how we can define an angular momentum in a spherically symmetric system, since angular momentum by definition chooses an axis of rotation. We circumvent this issue by asserting that, for a particular distribution, all particles have the same angular momentum, and that at every point in space we have an infinite number of infinitesimal particles rotating in every possible direction, such that every particle has a particle rotating opposite to it. In this way, spherical symmetry is preserved, but the dynamics of each particle are still influenced by angular momentum.

1.3   The Einstein-Vlasov System

The equation which describes the dynamics of our collisionless particles as they move through phase space is known as the Vlasov equation. The corresponding equation that describes how they interact through gravity is known as Einstein's equation. The system we study is therefore called the Einstein-Vlasov system.

A more mathematical treatment of the Einsten-Vlasov system than ours was initiated by Rendall and collaborators in a series of papers that primarily addressed the existence and uniqueness of solutions to the system, as well as the Cauchy problem [22, 2, 1]. The first numerical studies of critical phenomena were conducted by Rein, Rendall, and Schaeffer [12] using techniques motivated by previous work in numerical plasma physics. Subsequently, Olabarrieta and Choptuik [19, 20] numerically investigated critical phenomena in the system, also using a particle-based approach, and found evidence for Type-I pheonemena, including indications that the threshold solutions were static with near-critical solutions having lifetimes satisfying power law scaling of the form (1.1)

While these particle-based approaches indicated the existence of Type I critical phenomena, their relative poor accuracy and convergence properties left something to be desired. The implementation of a second order convergent code that indicates Type I critical phenomena is what this thesis provides, as well as results on the massless Einstein-Vlasov system, and the case of two separate distribution functions spanning a range of angular momenta.

CHAPTER 2

MATHEMATICAL FORMALISM

In this chapter, we define the set of equations that describe spherically symmetric collisionless matter interacting with itself only through its own net gravitational field. This system couples two equations: Einstein's equation and the Boltzmann equation for collisionless matter, also known as the Vlasov equation. The coupled system, which we will solve numerically, is thus

$$G_{\mu\nu} = 8\pi T_{\mu\nu} \tag{2.1}$$

$$\frac{df(t, x^k, p_k)}{d\sigma} = \frac{df(t, Rx^k, Rp_k)}{d\sigma} = 0 \qquad R \in SO(3) \tag{2.2}$$

The first equation, **Einstein's equation**, which relates the Einstein curvature tensor, $G_{\mu\nu}$, to the matter stress-energy tensor, $T_{\mu\nu}$, governs the geometric variables, while the second, the **Vlasov equation**, determines the evolution of a distribution function $f(t, x^k, p_k)$ in phase space. The evolution of the distribution function depends only on phase space variables and the geometry, so the problem reduces to solving an evolution equation with coupled constraints on the geometric variables. The exact system of equations will be explicitly presented in the following subsections.

To make notational conventions explicit: Latin indices $i, j, k, \cdots$ range over spatial dimensions (r,θ,ϕ), and Greek indices α, β, $\gamma, \cdots$ range over time and space (t,r,θ,ϕ). We use units where $G=c=1$. Primes, as in a', always denote

derivatives with respect to r. Overdots, as in $\dot{a}$ always denote derivatives with respect to time, t.

2.1 The 3+1 Formalism

We make use of the "3+1", or Arnowitt-Deser-Misner (ADM), formalism to decompose the 4 dimensional structure of spacetime defined by Einstein's equation into three spatial dimensions and one time dimension. The ADM formalism allows us to write Einstein's equation as a coupled set of constraint equations and evolution equations. In this section we closely follow the specific development of the ADM equations due to York [25], and paraphrased by Choptuik [5] in order to derive the relevant geometric equations for our system.

2.1.1 Foliation of Spacetime

We begin with an arbitrary 4 dimensional manifold $\mathcal{M}$ with metric g_{ab} and foliate it along level surfaces of a scalar field t into spacelike hypersurfaces Σ_t. These hypersurfaces are described locally by a *closed* one-form, Ω_a:

$$\Omega_a = \nabla_a t$$

The norm of Ω_a is:

$$g^{ab}\Omega_a\Omega_b = -\frac{1}{\alpha^2}$$

where α is known as the lapse. The unit-norm vector field dual to Ω_a is clearly,

$$n_a = -\alpha\Omega_a$$

Here we can think of n_a as being the 4-velocity field of a set of observers moving orthogonally to the slices, whose spatial coordinates, however, may in general

be changing.

Since n^a is orthogonal to the foliation, we can use it to define a **projection tensor**, $\gamma^a{}_b$, which we will later use to decompose tensors into components tangent and orthogonal to the hypersurfaces. We define the projection operator as:

$$\gamma^a{}_b = \delta^a{}_b + n^a n_b$$

If we operate with the projection tensor on our 4-metric, we obtain the **spatial metric**,

$$\gamma_{ab} = g_{ab} + n_a n_b$$

that is, γ_{ab}, is the metric induced on the hypersurfaces. Note that this tensor is also the completely covariant form of the projection tensor (i.e. the version of the projection tensor that has all indices downstairs). Furthermore, note that the relative $+$ sign in front of $n_a n_b$, in both of the above definitions, is due to the Lorentzian signature, $(-+++)$, we demand of our spacetimes.

On our three dimensional hypersurfaces, we have a natural definition of the 3-derivative as the projection of the covariant derivative,

$$D_a = \gamma^b{}_a \nabla_b$$

This definition allows us to introduce the spatial **Riemann tensor**, which can be defined by its action on an arbitrary dual-vector, ω_a,

$${}^3\mathcal{R}_{abc}{}^d \omega_d = (D_a D_b - D_b D_a)\omega_c$$

We also have the spatial Ricci tensor,

$$^3\mathcal{R}_{ac} = ^3\mathcal{R}_{abc}{}^b$$

and finally the spatial Ricci scalar,

$$^3\mathcal{R} = ^3\mathcal{R}^a_a$$

We now define the **extrinsic curvature**, K_{ab}, which will help in formulating Einstein's equations. K_{ab} describes how the 3 dimensional hypersurfaces are embedded in the 4 dimensional spacetime by accounting for the variation of the surface normal gradient, when projected onto the three dimensional hypersurface. The extrinsic curvature is also closely related to the variable conjugate to the spatial metric, when Einstein's theory is cast in Hamiltonian form.

Specifically, we have

$$K_{ab} \equiv -D_a n_b = \nabla_a n_b - n_a n^c D_c n_b$$

It can also be shown that the extrinsic curvature can be written in terms of the Lie derivative of the spatial metric along the normal field,

$$K_{ab} = -\frac{1}{2}\mathcal{L}_n \gamma_{ab}$$

The geometry of the spacetime has now been entirely defined. The spatial metric describes the curvature of spacelike hypersurfaces, while the extrinsic curvature describes how these surfaces are embedded in the spacetime.

Examination of Einstein's equation (2.1), reveals that it generically decomposes into (1) a set of evolution equations for the dynamical variables (components of the spatial metric and extrinsic curvature tensors), and (2) a set of

constraint equations on the dynamical variables.

In order to derive the 3+1 form of the Einstein equation, we will act with the normal vector and projection tensor on (2.1). Combining contractions with the normal vector and projections onto the foliations will yield three groups of equations: the Hamiltonian constraint (1 equation), the momentum constraint (3 equations), and evolution equations for the extrinisic curvature components (6 equations).

In looking at Einstein's equation (2.1), we first turn our attention to the right hand side, and the behavior of the **stress-energy tensor**, T_{ab}. Under the operations of contraction with the normal and projection onto the hypersurface, T_{ab} will define a set of physical quantities related to the matter content of the system with respect to observers who are moving orthogonally to the slices.

Contracting the stress-energy tensor twice with the normal vector, produces the energy density:

$$\rho = n^a n^b T_{ab}$$

while contracting and projecting produces the momentum density:

$$j^a = \gamma^a{}_b n_c T^{bc}$$

Finally, projecting all indices yields the stresses in the hypersurface:

$$S^{ab} = \gamma^a{}_c \gamma^b{}_d T^{cd}$$

Now, application of similar contractions and projections to the left hand side of Einstein's equation (i.e. to the Einstein tensor) produces the basic sets of equations that we are to solve.

Contracting Einstein's equation twice with the normal vector produces the

Hamiltionian constraint:

$$G_{ab}n^a n^b = T_{ab}n^a n^b \qquad (2.3)$$

$$^3\mathcal{R} + K^2 - K_b^a K_a^b = 16\pi\rho$$

where $K = g^{ab}K_{ab}$.

Contracting once and projecting produces the **momentum constraint**:

$$\gamma^a{}_c G^{cb} n_b = \gamma^a{}_c T^{cb} n_b \qquad (2.4)$$

$$D_b K^{ab} - D^a K = 8\pi j^a$$

Finally, projecting Einstein's equation onto the hypersurfaces produces an evolution equation for the extrinsic curvature components:

$$\gamma^a{}_c \gamma^b{}_d G^{cd} = \gamma^a{}_c \gamma^b{}_d T^{cd} \qquad (2.5)$$

Note that the Hamiltonian and momentum constraints involve only spatial derivatives of the dynamical variables, and therefore represent equations which much be satisfied on each hypersurface. In contrast, as the name implies, the evolution equations (2.5) are simply that—evolution equations for the extrinsic curvature compoents, as will be sketched below.

At this point, however, we must first introduce a coordinate system and an associated coordinate basis in which to derive specific forms for our equations.

To do this, we consider the Lie derivative along a vector field, t^a, tangent to lines of constant spatial coordinate

$$t^a = \frac{d}{dt}^a = \alpha n^a + \beta^a$$

Here α is the lapse function introduced earlier. β^a is known as the shift vec-
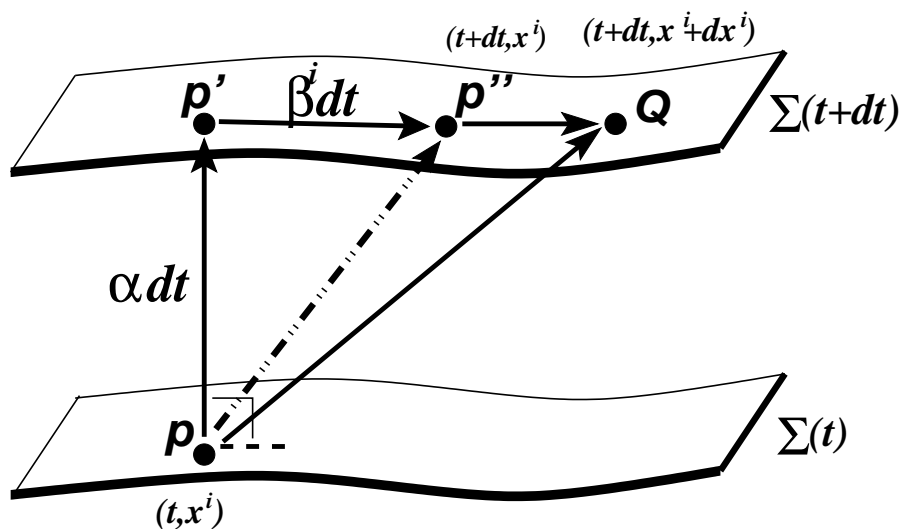
Figure 2.1: Quantities involved in the 3+1 decomposition of a four dimensional manifold, with metric $g_{\mu\nu}$. Credit: Kevin Lai.

tor, and encodes the "shifting" of spatial coordinates relative to normal propagation (see Fig. 2.1). In a 3+1 coordinate system, (t, x^i), we can then express the 3+1 form of the spacetime line-element using a 4-dimensional version of the Pythagorean theorem:

$$ds^2 = (-\alpha^2 + \beta^j \beta_j)dt^2 + 2\beta_j dx^j dt + g_{ij} dx^i dx^j$$

Having adopted coordinates (t, x^i), the evolution of the spatial metric, can be derived from the Lie derivative of the metric with respect to time,

$$\mathcal{L}_t \gamma_{ab} = -2\alpha K_{ab} + \mathcal{L}_\beta \gamma_{ab} \tag{2.6}$$

Extensive manipulation of (2.5), using (2.6), then allows us to write the

evolution of the extrinsic curvature as:

$$\mathcal{L}_t K^a_b = \mathcal{L}_\beta K^a_b - D^a D_b \alpha + \alpha \left\{ {}^3\mathcal{R}^a_b + K K^a_b + 8\pi \left[\frac{1}{2} \gamma^a{}_b (S^c{}_c - \rho) - S^a_b \right] \right\} \quad (2.7)$$

Worthy of note is the fact that though a symmetric 4-dimensional metric ostensilby has 10 degrees of freedom, 4 of these (the lapse and shift vector components) will be determined by our choice of coordinates. Furthermore, another 4 will be fixed by the constraint equations, leaving only 2 degrees of freedom, which are the "true" dynamical degrees of freedom of the gravitational field. Note, however, that we have 6 evolution equations each for the metric (2.6) and extrinsic curvature (2.7). We therefore have a great deal of flexibility in terms of precisely which equations we wish to use in order to update our geometrical variables. Indeed, due to (1) our restriction to spherical symmetry and (2) our use of a specific spherical coordinate system, we can eschew any need to solve evolution equations and, rather, implement what is known as a completely constrained evolution.

We now proceed to choose a set of coordinates in spherical symmetry and derive explicit, coordinate dependent forms of the needed constraint and evolution equations.

2.2   Polar-Areal Coordinates in Spherical Symmetry

We now choose to impose spherical symmetry on our system, and then adopt **polar-areal coordinates** to analyze its dynamics. The most general spherically-symmetric metric can be written as:

$$ds^2 = (-\alpha + a^2\beta^2)dt^2 + 2a^2\beta dt dr + a^2 dr^2 + r^2 b^2 d\Omega^2$$

where α, a, β, and b are functions of r and t.

The polar-areal choice of coordinates results from two conditions, namely polar slicing and the areal radius condition. The former condition determines the structure of the extrinsic curvature. In particular, polar slicing implies:

$$K = K^i{}_i = K^r{}_r$$

The areal radius condition, requires the proper surface area of a sphere of radius r to be $4\pi r^2$; that is, that $b(t,r) \equiv 1$. One can then show that the slicing condition and the areal radius condition further imply that the metric is diagonal, i.e. that $\beta(t,r) = 0$, so, solely because of the spherical symmetry, and the very special properties of these coordinates (which generalize those of the original Schwarzschild solution), we eliminate 3 of the geometric variables (i.e. b, β and the extrinisic curvature component $K^\theta{}_\theta$) in this case.

Thus, our line element now reads

$$ds^2 = -\alpha^2(t,r)dt^2 + a^2(t,r)dr^2 + r^2 d\Omega^2 \tag{2.8}$$

and the spacetime metric is fully fixed by knowledge of the two functions $\alpha(t,r)$ and $a(t,r)$, which will be calculated from the slicing condition and Hamiltonian constraint, respectively. We now derive the exact form of these two equations, using (2.3) and (2.5).

Using our 3+1 coordinate system, and taking the form of the metric (2.8) we can calculate (2.3) by noting that:

$$G_{ab} = R_{ab} - \frac{1}{2}Rg_{ab}$$

where, R_{ab} is the Ricci tensor, defined as,

$$R_{ac} = R_{abc}{}^{b}$$

and

$$R_{abc}{}^{d} = \partial_{b}\Gamma^{d}{}_{ac} - \partial_{a}\Gamma^{d}{}_{bc} + \Gamma^{e}{}_{ac}\Gamma^{d}{}_{eb} - \Gamma^{e}{}_{bc}\Gamma^{d}{}_{ea}$$

The $\Gamma^{a}{}_{bc}$ are known as the **Christoffel symbols** and are easily calculated from derivatives of the metric (2.8), via the equation:

$$\Gamma^{a}{}_{bc} = \frac{1}{2}g^{ad}(\partial_{b}g_{cd} + \partial_{c}g_{bd} - \partial_{d}g_{bc})$$

For our particular metric, the Christoffel symbols are tabulated in Appendix A.

Upon calculating the Einstein tensor for our particular metric, and contracting Einstein's equation with the hypersurface normal twice, we find that (2.3) becomes

$$\frac{a'}{a} = \frac{1 - a^2}{2r} - \frac{ra^2}{2}8\pi T^{t}_{t} \tag{2.9}$$

which is the final form of our Hamiltonian constraint.

To derive the slicing condition we first note that if we assume that $K(r, 0) \equiv K^{r}{}_{r}(r, 0)$—i.e. that the slicing condition holds at the initial time—then we must have $K^{\theta}{}_{\theta}(r, 0) = 0$ since $K \equiv K^{i}{}_{i} = K^{r}{}_{r} + K^{\theta}{}_{\theta} + K^{\phi}{}_{\phi} = K^{r}{}_{r} + 2K^{\theta}{}_{\theta}$. Thus, to ensure that the slicing condition be maintained in time, it is sufficient to demand that

$$\dot{K}^{\theta}{}_{\theta}(t, r) = 0$$

for all r and for all $t \geq 0$. Use of the corresponding component of the evolution equations (2.5)—now interpreted as an equation for the lapse function, $\alpha(t, r)$—

leads to the final form of our slicing condition:

$$\frac{\alpha'}{\alpha} = \frac{a^2 - 1}{2r} + \frac{ra^2}{2} 8\pi T^r_r \tag{2.10}$$

Note that this equation is to be solved subject to (1) regularity at the origin (i.e. no "kinks" in the slices), thus $\lim_{r \to 0} \alpha(t, r) = \alpha_0(t) + r^2 \alpha_2(t) + O(r^4)$, which implies $\alpha'(0, t) = 0$. (2) asymptotic flatness and identification with t with inertial proper time at infinity, which implies $\lim_{r \to \infty} \alpha(t, r) = 1$.

As is evident from (2.9) and (2.10), we can now determine the two residual degrees of freedom in the metric by solving two coupled ordinary differential equations. The method used to solve this couple system is discussed in Chapter 3.

2.3 The Vlasov Equation

Each component particle of collisionless matter in spherical symmetry has an associated radial position, r, and radial momentum, p_r; therefore a distribution of particles can be represented in a two dimensional phase-space by a distribution function, $f(t, r, p_r)$. **Liouville's theorem** says that if the particles are non-interacting, then the distribution function in phase space is a conserved quantity and we have

$$\frac{df}{d\sigma} = 0 \tag{2.11}$$

where σ is an affine parameter along a particle's trajectory. The trajectories in phase space are tangent to the Liouville operator, which as an expression of $d/d\sigma$'s action on f is

$$\mathcal{L} = p^\mu \frac{\partial}{\partial x^\mu} - \Gamma^i_{\mu\lambda} p^\mu p^\lambda \frac{\partial}{\partial p^i} \tag{2.12}$$

If particles are moving in the θ or ϕ directions, clearly their trajectories cannot be represented in a two-dimensional phase space. However, if we now define each "particle" as representing a shell of an infinite number of infinitesimal particles each orbiting $r = 0$ with some net angular momentum of magnitude $|l|$, but in every possible direction, then the "particle" distribution *can* still be described within a two-dimensional phase space. In this case the average angular momentum is zero, and we maintain spherical symmetry and indeed simplicity, but clearly the average of the square of the angular momentum is non-zero. Therefore we may expect a term proportional to l^2 to influence the dynamics, and indeed it does.

We note here that previous studies have actually worked within the context of the full 3D phase space, i.e. with $f \equiv f(t, r, p_r, l^2)$. Here, we choose to reduce the computational burden by treating l^2 as a parameter that can be varied, but that which, for any fixed computation, will be set to some fixed value.

We observe that this implies that for any specific calculation, all of the particles have the *same* angular momenta. Intuitively, not least since the angular momentum must be conserved *particle by particle*, we feel that this lack of a spread in angular momentum space (we effectively only compute with δ-function-in-l^2 conditions in this work) should have little impact on the overall picture of criticality in the model. Moreover, we partially test the validity of the "frozen l^2" ansatz in Chap. 6 in our study of two species of particles each of which has a *distinct* value of l^2, and where the picture of criticality *does* appear to be basically the same as for the single species calcuations.

The "equation of motion" that determines trajectories of our particles can be explicitly calculated by applying the Liouville operator to the distribution function:

$$\frac{df}{d\sigma} = \mathcal{L}(f) = 0 \tag{2.13}$$

This is the Vlasov equation, and it determines the time-evolution of our matter in phase space. Given the choice (2.8) for our metric, we obtain after some algebra that

$$\frac{\partial f}{\partial t} + \frac{\alpha p_r}{a^2 \bar{p}^t} \frac{\partial f}{\partial r} + \left(-\alpha' \bar{p}^t + \frac{\alpha}{a^3} a' \frac{p_r^2}{\bar{p}^t} + \frac{\alpha l^2}{\bar{p}^t r^3} \right) \frac{\partial f}{\partial p_r} = 0 \tag{2.14}$$

where we define

$$\bar{p}^t = \alpha p^t = \sqrt{m^2 + (ap^r)^2 + l^2/r^2}$$

Note that other authors [12, 13] denote $\bar{p}^t$ by W and relate it to the constant of motion, l^2, which is called F in their notation.

To expedite the discussion in Sec. 3, it is convenient to define auxiliary functions $g \equiv g(t, r)$ and $h \equiv h(t, r)$ as follows:

$$g = \frac{\alpha p_r}{a^2 \bar{p}^t} \tag{2.15}$$

$$h = -\alpha' \bar{p}^t + \frac{\alpha}{a^3} a' \frac{p_r^2}{\bar{p}^t} + \frac{\alpha l^2}{\bar{p}^t r^3} \tag{2.16}$$

With the these definitions, the Vlasov equation can be written in the simple form

$$\frac{\partial f}{\partial t} + g \frac{\partial f}{\partial r} + h \frac{\partial f}{\partial p_r} = 0 \tag{2.17}$$

which makes the precise differential form of the equation—which specific derivatives must be approximated—transparent.

2.4   The Stress Energy Tensor for Collisionless Matter

At this stage, we have expressions for the evolution of the distribution function (2.13) and the geometric constraints (2.9–2.10) that must be satisfied. The only remaining part of these equations that needs to be worked out in detail are certain components of the stress-energy tensor, $T^{\mu\nu}$. For collisionless matter we have that the stress-energy tensor is just the integral over all collisionless particles in phase-space that comprise the system, with the fundamental quantity being integrated simply being the outer product of the particle's 4-momentum, p^{μ}, with itself:

$$T^{\mu\nu}(r) = \int dV_p \frac{1}{m} p^{\mu} p^{\nu} f(t, r, p^r, l^2) \tag{2.18}$$

Here dV_p represents an integral over the entire momentum volume of phase space. After introducing coordinates adapted to the symmetry [24], we find

$$dV_p = m \frac{dp_r dl^2 d\psi}{2ar^2 \bar{p}^t}$$

The required stress-energy components for our constraint equations are thus

$$T^t_t = -\frac{\pi}{a^2 r^2} \int \bar{p}^t f(t, r, p_r, l^2) dp_r dl^2 \tag{2.19}$$

$$T^r_r = \frac{\pi}{a^2 r^2 \alpha} \int p_r f(t, r, p_r, l^2) dp_r dl^2 \tag{2.20}$$

2.5   Conserved Quantities

We now derive two diagnostic quantities that will be useful in providing "single number" views of convergence. Indeed, due to our restriction to spherical symmetry and asymptotic flatness, we know that of the 4 conserved ADM

"charges"—ADM mass and ADM 3-momentum—only the ADM mass, M_∞, can be non-trivial. Thus, the ADM mass is *always* absolutely conserved in time given our assumptions. Therefore, both of the diagnostic quantities defined below, being absolutely conserved in time in the limit that the discretization scale, h, goes to 0, and both measuring mass content of the system, must tend to M_∞ as $h \to 0$. However, as will be seen below, the expressions for the two distinct approximate measures of M_∞ are quite different, both in terms of which of the dynamical variables they directly depend on, as well as in terms of what types of numerical approximations are made in their approximate computation.

In addition, purely for historical reasons (vis a vis development of this project), we will refer to the two estimates of the ADM mass, M_∞, as "the ADM mass" (or just "the mass") and "the energy" respectively.

2.5.1   ADM Mass: Direct Computation

Due to our restriction to spherical symmetry and our choice of polar-areal coordinates (which are clearly a natural generalization of the usual Schwarzschild coordinates to time-dependent, spherically-symmetric spacetime), Birkhoff's theorem ensures that in a vacuum region—in our case, outside the *radial* support of the distribution function $f(t, r, p^r)$—the metric is precisely

$$ds^2 = -\left(1 - \frac{2M}{r}\right)dt^2 + \left(1 - \frac{2M}{r}\right)^{-1} dr^2 + r^2 d\Omega^2$$

where M is the gravitating mass of the energy-denstity within the radius r (as in Newtonian gravity, observers at any $\tilde{r}$ in spherical symmetry feel no gravity due to matter located at distance $r > \tilde{r}$).

$$a^2(t, r) \quad \rightarrow \quad \left(1 - \frac{2M}{r}\right)^{-1} \tag{2.21}$$

$$\alpha^2(t,r) \quad \rightarrow \quad \left(1 - \frac{2M}{r}\right) \tag{2.22}$$

Indeed, it is conventional when using polar-areal coordinates to define the so called **mass aspect function**, denoted here $M(t,r)$, by identification of the line elements (2.8) and (2.5.1)

$$M(t,r) = \frac{1}{2}r\left(1 - a^{-2}\right) \tag{2.23}$$

Note that the mass in this case is an *algebraic* function of the geometric variables, and indeed, is a function only of the radial metric function, a.

In the limit that $r \to \infty$, one can read off the ADM mass from the mass aspect function:

$$\lim_{r\to\infty} M(t,r) = M_{\mathrm{ADM}} \tag{2.24}$$

2.5.2 Total Energy (Indirect computation of the ADM mass)

A second, somewhat independent computation of the ADM mass comes from a direct integration of the energy content—due to the particle matter—of the spacetime. Our distribution function lives in a 2D phase space, and, as (2.19) illustrates, various quadratures of the distribution function over phase space represent various components of the stress-energy tensor. Using (2.19), we can derive an expression for the scalar energy density in the system:

$$\rho = n^a n^b T_{ab} = \frac{\pi}{a^2 r^2} \int \bar{p}^t f(t,r,p_r,l^2) dp_r dl^2$$

Integrating this over all p_r and r in our system yields what we call "the total energy" in the system, which as argued above, must also tend to, M_∞, in the continuum limit, $h \to 0$, if our code is convergent.

2.6   The Equations, Summarized

As previously mentioned, given an initial distribution of matter in the form of $f(0, r, p_r, l^2)$, the Vlasov equation, (2.14) determines the time evolution of f according to:

$$\frac{\partial f}{\partial t} + \frac{\alpha p_r}{a^2 \bar{p}^t}\frac{\partial f}{\partial r} + \left(-\alpha'\bar{p}^t + \frac{\alpha}{a^3}a'\frac{p_r^2}{\bar{p}^t} + \frac{\alpha l^2}{\bar{p}^t r^3}\right)\frac{\partial f}{\partial p_r} = 0 \qquad (2.25)$$

However, to determine the time evolution, the metric coefficients $a(t, r)$ and $\alpha(t, r)$ must be known. These are fixed using the Hamiltonian constraint and slicing condition as discussed above:

$$\frac{a'}{a} = \frac{1 - a^2}{2r} - \frac{ra^2}{2}8\pi T_t^t \qquad (2.26)$$

$$\frac{\alpha'}{\alpha} = \frac{a^2 - 1}{2r} + \frac{ra^2}{2}8\pi T_r^r \qquad (2.27)$$

Now, these equations depend on two specific components of the stress-energy tensor, $T^{\mu\nu}$, which are

$$T_t^t = -\frac{\pi}{a^2 r^2}\int \bar{p}^t f(t, r, p_r, l^2)dp_r dl^2 \qquad (2.28)$$

$$T_r^r = \frac{\pi}{a^2 r^2 \alpha}\int p_r f(t, r, p_r, l^2)dp_r dl^2 \qquad (2.29)$$

Notice that the two stress-energy components are not independent of the geometry, so that their calculation and the calculation of the metric coefficients must be done in a self-consistent manner. This will later be referred to as the coupled stress-energy, metric-coefficient problem. The methods for solving this, as well as those for solving the evolution and constraint equations, are described in the following chapter.

CHAPTER 3

NUMERICS

Advances in computational power and resources since the 1970's allow us to directly solve for a distribution function's evolution in the spherically symmetric 3+1 Einstein Vlasov system. Since this method was once computationally intractable, researchers were led to less computationally expensive methods, typically based on Monte Carlo integration of the Vlasov equation, and finite difference treatment of the geometric variables [24, 12, 19, 20], to yield an approximation. The great advantage of the "direct" approach that we have implemented and that is discussed in this chapter, is that the discrete solutions we generate have the usual sort of convergence behaviour that one expects for finite difference approximations to smooth solutions of partial differential equations.

A quick analysis of a finite difference approach shows why Shapiro and Teukolsky were lead to use Monte Carlo methods in their pioneering work [7]. Assuming we have 3+1 dimensions, and an equal number of points, N, required to resolve each dimension, then the computational cost, denoted $C_C^{\mathrm{FD}}(N)$ of the calculation scales as

$$C_C^{\mathrm{FD}}(N) \sim N^4$$

while the memory requirements, $C_M^{\mathrm{FD}}(N)$, scale as

$$C_M^{\mathrm{FD}}(N) \sim N^3$$

Immediately we see that even a poorly resolved hypercube, with 100 points

on an edge, would lead to memory requirements on the order of megabytes and computational requirements on the order of hundreds of megaflops—unavailable even on the supercomputers and "big iron" mainframes of those days.

Shapiro and Teukolsky's simplifying Monte Carlo technique represented the distribution function in three dimensional phase space by a collection of M phase-space particles, whose initial distribution in (r, p_r, l) are defined pseudo-randomly via a Monte-Carlo method, typically the rejection method [24]. M dominantly affects the accuracy of the solution, and from the law of large numbers, we can expect the following asymptotic behavior of our solution for $f = f(t, r, p_r, l)$

$$\lim_{M \to \infty} f = \hat{f}^{\mathrm{MC}} + \hat{E}^{\mathrm{MC}}_{\sqrt{\cdot}} M^{1/2} + \text{higher order terms}$$

Note that f represents the continuum distribution function, and $\hat{f}^{\mathrm{MC}}$ is the Monte-Carlo-generated approximate solution. $\hat{E}^{\mathrm{MC}}_{\sqrt{\cdot}}$ is the leading order error function.

While the Monte-Carlo method reduces the computational complexity of the problem to $O(M)$ by allowing us to integrate the phase-space trajectories of M particles in time, the leading order error terms are not necessarily smooth and therefore give us no extrapolatable additional information as to the higher order behavior of the solution.

In contrast, the finite difference (finite volume) case yields solutions of the following form (assuming completely centred differencing, as we have attempted to implement):

$$\lim_{h \to 0} f = \hat{f}^{\mathrm{FD}} + h^2 \hat{e}^{\mathrm{FD}}_2 + O(h^4) \tag{3.1}$$

with the critical facts that

1. $\hat{e}^{\mathrm{FD}}_2$ has smoothness properties similar to f.

2. Straightforward convergence tests can assess to what degree (3.1) is valid, and thus one can easily put *reliable* error bars on the solution.

3. Since the error functions, $\hat{e}_2^{\mathrm{FD}}$, $\hat{e}_4^{\mathrm{FD}} \cdots$ *are* expected to be smooth, it is much easier to identify, and argue for, continuum properties, such as an entire function, $\zeta(t, r)$, identically vanishing, for all r and for some range of t, as happens to the time dervatives of *all* dynamical variables in the apparently static solutions of the Einstein-Vlasov system that we identify below.

3.1 The 2+1 Ansatz

The computational complexity of computing a discrete solution of the Einstein-Vlasov system using finite volume techniques can be further reduced from $O(N^4)$ to $O(N^3)$ by adopting the ansatz that all particles have the same squared angular momentum, l^2. In other words, the distribution is either a δ-function, or a sum of δ-functions, in l^2, resulting in a 2-dimensional phase-space (r, p_r). This approach is new, and was suggested by Choptuik [8].

As discussed previously, we argue that this ansatz is justified since particles cannot exchange angular momenta, even through their combined gravitational field. This is readily apparent if we note that the final form of the Vlasov equation 2.14 contains no "velocities" in the l-direction. Thus, any distribution is initially and **remains** a sum of δ-functions in l, whose phase-space volumes are independently conserved. As a test, we will analyze the sum of two δ-functions in l and show that the critical results are universal in the sense of *not* disappearing when we use two δ-functions. This provides at least some evidence that our ansatz is indeed justified.

3.2   Finite Volume Methods

Finite volume methods take advantage of flux-conservation in cells defined on a grid over a computational domain [15]. A 2-dimensional hyperbolic equation is said to be in **flux-conservative form** if it can be written as

$$\frac{\partial q}{\partial t} + \frac{\partial F_x(q)}{\partial x} + \frac{\partial F_y(q)}{\partial y} = 0 \tag{3.2}$$

In this form, the quantities $F_{x,y}(q)$ are two distinct functions of q known as **fluxes**, and (3.2) expresses a conservation law.

If we divide a computational domain into a grid which is N_x cells of width $\Delta x \times N_y$ cells of height Δy, then the average value in cell (i,j) is

$$Q_{ij}^n = \frac{1}{\Delta x \Delta y} \int_{C_{ij}} \int_{C_{ij}} q(x,y,t)\,dxdy \tag{3.3}$$

where C_{ij} denotes an integral over the i,j^{th} cell, and n indexes time. We can write (3.2) for each cell in integral form,

$$\begin{aligned}
\frac{d}{dt} \int_{C_i} \int_{C_i} q(x,y,t)dxdy \quad &= \\
\int_{y_b}^{y_t} F_x(q(x_l,y,t))dy \quad &- \quad \int_{y_b}^{y_t} F_x(q(x_r,y,t))dy \\
+ \int_{x_l}^{x_r} F_y(q(x,y_b,t))dx \quad &- \quad \int_{x_l}^{x_r} F_y(q(x,y_t,t))dx
\end{aligned} \tag{3.4}$$

where subscripts l, r, b and t describe values at the left, right, bottom and top boundaries, respectively, of cell (i,j). The above equation is merely a statement that, if flux is conserved, the change in the cell value will be equal to the sum of fluxes into and out of the cell.

Dividing (3.4) by $\Delta x \Delta y$ and substituting in (3.3) yields an equation for the

future cell value

$$Q_{ij}^{n+1} = Q_{ij}^n - \frac{\Delta t}{\Delta x}\left(F_{x,r}^n - F_{x,l}^n\right) - \frac{\Delta t}{\Delta y}\left(F_{y,b}^n - F_{y,t}^n\right) \qquad (3.5)$$

The problem then reduces to accurately computing the *average* fluxes $F_{x,l}^n$ and $F_{x,r}^n$, at the left and right boundaries, respectively, as well as those at the bottom and top boundaries, namely $F_{y,b}^n$ and $F_{y,t}^n$. A variety of methods exist for estimating the fluxes, one of the more promising for fluid dynamics simulations being High Resolution Shock Capturing (HRSC) techniques.

If steep gradients are produced, HRSC methods provide second order convergence in domains excluding maxima, and first order convergence near maxima, while still resolving shocks. It has been shown [24] that the Einstein-Vlasov system can develop significant mixing and steep gradients, so the use of HRSC in a finite volume method seems natural. We choose to use a min-mod slope limiter [15] for flux estimation, and show details of the convergence of our scheme in Chap. 5.

We now proceed to show that the Vlasov equation *can* be written in flux-conservative form, and then describe a finite volume approach that makes use of an HRSC scheme to implement the evolution of the distribution function. Finally, we make a note on an iterative method used to solve the coupled stress-energy, metric-coefficient problem described at the end of Section 2.

3.3   Casting the Vlasov Equation in Flux-Conservative Form

In the numerical study of the Einstein-Vlasov system, it does not appear to be widely known that the Vlasov equation can be cast into flux-conservative form [12, 24, 19], for which finite volume techniques are ideally suited. We now

perform a simple demonstration that the Vlasov equation (2.17), *can* be written in that form.

Currently, the Vlasov equation is

$$\frac{\partial f}{\partial t} + g\frac{\partial f}{\partial r} + h\frac{\partial f}{\partial p_r} = 0$$

with g and h defined by (2.15) and (2.16), respectively. We wish to recast this equation in the form

$$\frac{\partial f}{\partial t} + \frac{\partial(gf)}{\partial r} + \frac{\partial(hf)}{\partial p_r} = 0 \qquad (3.6)$$

in order for it to be expressed as a conservation law, (3.2). One possible way for this to hold is if g and h are independent of r and p_r, respectively. However we immediately see that this is not the case. Another possible condition is to have

$$\frac{\partial g}{\partial r} = -\frac{\partial h}{\partial p_r}$$

and this *is* satisfied. Therefore, we can correctly identify the quantities gf and hf as fluxes in the r and p_r directions, respectively, by writing the Vlasov equation in the form (3.6).

3.4 Finite Volume Implementation for the Evolution

With the Vlasov equation in flux-conservative form, second order in time evolution is accomplished by a two step Euler method implementation of (3.5). Denoting the distibution function at time n by f^n and fluxes in the r and p_r directions at time n as F_r^n and $F_{p_r}^n$, respectively, we briefly describe the two-step Euler method for advancing the solution in time: First, the fluxes at the current

time are used to advance the distribution function one half timestep, to $f^{n+\frac{1}{2}}$. At this point we calculate the half-advanced fluxes $F_r^{n+\frac{1}{2}}$ and $F_{p_r}^{n+\frac{1}{2}}$, and use these, instead of the fluxes at time n, to update f^n to f^{n+1}. This produces a second order in time algorithm.

3.5 Solving the Constraint Equations

In order to determine the form of our metric functions on each hypersurface, we need to solve the constraint equations. Solving the Hamiltonian constraint,

$$\frac{a'}{a} = \frac{1-a^2}{2r} - \frac{ra^2}{2} 8\pi T_t^t \tag{3.7}$$

with the regularity condition

$$\lim_{r \to 0} a(t,r) = 1 + r^2 a_2(t) + O(r^4)$$

that follows from local flatness at the origin, at any time, t, yields $a(t,r)$, which can then be used in the slicing equation

$$\frac{\alpha'}{\alpha} = \frac{a^2-1}{2r} + \frac{ra^2}{2} 8\pi T_r^r \tag{3.8}$$

to solve for $\alpha(t,r)$ at that time.

We solve 3.8 by integrating inwards from $r = r_{\max}$ with the condition that

$$\alpha(r_{\max}) = \frac{1}{a(r_{\max})}$$

This last condition follows for the known (Schwarzschild) form of the vacuum spherically symmetric line element in our coordinates, plus the demand that time at infinity measure local proper time for an inertial observer, also at spatial

infinity.

3.6 An Iterative Solution of Einstein's Equation

We now discuss an iterative method for solving the coupled stress-energy, metric-coefficient problem mentioned in Section 2. As described, the constraint equations for $a(t, r)$ and $\alpha(t, r)$ depend on the stress-energy components T_r^r and T_t^t, which themselves depend on $a(t, r)$ and $\alpha(t, r)$.

Defining a set of solutions for the stress-energy tensor at iteration i by $\mathcal{T}^i$, and a set of solutions for the geometric variables at iteration i by $\mathcal{G}^i$, then an algorithm yielding consistent $\mathcal{T}^i$ and $\mathcal{G}^i$ for a distribution function f at a particular time is:

- Define $\mathcal{G}^0$ as the flatspace set of solutions.

- Calculate $\mathcal{T}^0\left[\mathcal{G}^0\right]$

- while $(|\mathcal{T}^i\text{-}\mathcal{T}^{i-1}| > \textbf{tol})$ AND $(|\mathcal{G}^i\text{ - }\mathcal{G}^{i-1}| > \textbf{tol})$

    1. Calculate $\mathcal{T}^i\left[\mathcal{G}^i\right]$

    2. Calculate $\mathcal{G}^i\left[\mathcal{T}^i\right]$

3.7 A Portrait of the Program Flow

Here, we briefly summarize the flow of the program for quick reference. The program solves the Einstein-Vlasov system by iteratively evolving a distribution function, $f(t) \rightarrow (t + \Delta t)$, or, equivalently $f^n \rightarrow f^{n+1}$

1. Define an *initial* distribution $f(t, r, p_r)$ of compact support.

2. Iteratively solve for $\mathcal{T}(t)$ and $\mathcal{G}(t)$.

3. Calculate average fluxes and advance the solution to $f(t + \Delta t/2)$.

4. Iteratively solve for $\mathcal{T}(t + \Delta t/2)$ and $\mathcal{G}(t + \Delta t/2)$.

5. Calculate the average fluxes $F_r(t + \Delta t/2)$ and $F_{p_r}(t + \Delta t/2)$.

6. Calulate $f(t + \Delta t)$ using $F_r(t + \Delta t/2)$ and $F_{p_r}(t + \Delta t/2)$.

7. Use $f(t + \Delta t)$ as the initial distribution in step 1.

CHAPTER 4

CONVERGENCE AND CONSERVATION TESTS

4.1 Convergence

Here we show sample convergence plots for both the metric functions and the stress-energy tensor components for an arbitrary "test scenario". The evidence suggests that our code is not yet second order accurate, even well away from extrema in the dynamical variables, and this matter is still under investigation. Nonetheless, we do have convincing evidence that the code *is* converging to the continuum solution in all cases, if only at first order, $O(h)$.

To perform a convergence test, one must calculations at three or more resolutions that use the same initial configuration. We label the distinct resolutions used by h_i, so that if the cell width at the coarsest level, h_1, is Δx, then the width of a cell at level i is $2^{-(i-1)}\Delta x$. With each level we double the number of cells in a particular direction. In two dimensions we therefore quadruple the total number of cells in going from a level i calculation to a level $i+1$ one.

A convergence analysis verifies the fact that, when discretising a solution to second order—so that the truncation error is second order—the expected error in the approximate solution is also $\mathcal{O}(\Delta x^2)$ [6]. Therefore, if our code is indeed second order, we should find that the deviation between our closest approximation to a continuum solution, h_3, and the next-closest, h_2 is one

quarter the error between h_2 and h_1. Alternatively, four times $h_3 - h_2$ should be about equal to $h_2 - h_1$. Results from such as test are plot in Figs. 4.1 and 4.2 for the stress-energy component T_r^r and the metric function $a(t, r)$. The convergence tests are done at two different times to show that convergence is achieved throughout the duration of an evolution. Note that the largest discrepancy appears near peaks, since the min-mod limiter is first-order near local extrema, and we should therefore expect the difference $h_3 - h_2$ to be only half of $h_2 - h_1$.

Again, it is important to note that although Figs. 4.1 and 4.2 show clearly that the code *is* converging, they do *not* provide convincing evidence of $O(h^2)$ convergence, even away from extrema, and understanding of this non-optimal behaviour will require further study.
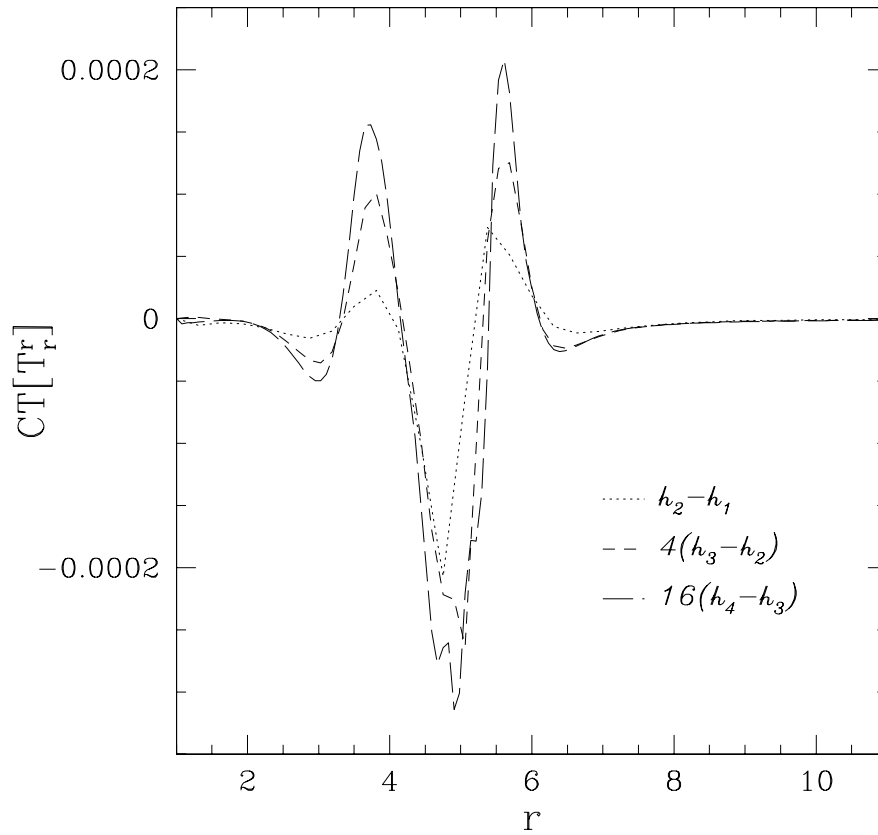
4.2 Mass and Energy Conservation

The total mass and energy quantities defined previously (recall that both should tend to the ADM mass in the continuum limit) are valuable diagnostics precisely because their conservation is a necessary property of the continuum solution. If a solution's total mass is not conserved as the fundamental mesh scale, h, tends to 0, then one can be certain the code is not solving the Einstein-Vlasov system.

Again, to recap the previous discussion, we monitor conservation of the ADM mass in two *independent* ways. In the first instance, we read off the ADM mass from the large r behaviour of the mass aspect function, $M(t, r)$:

$$M(t, r) = \frac{r}{2} \left(1 - \frac{1}{a^2(t, r)} \right)$$
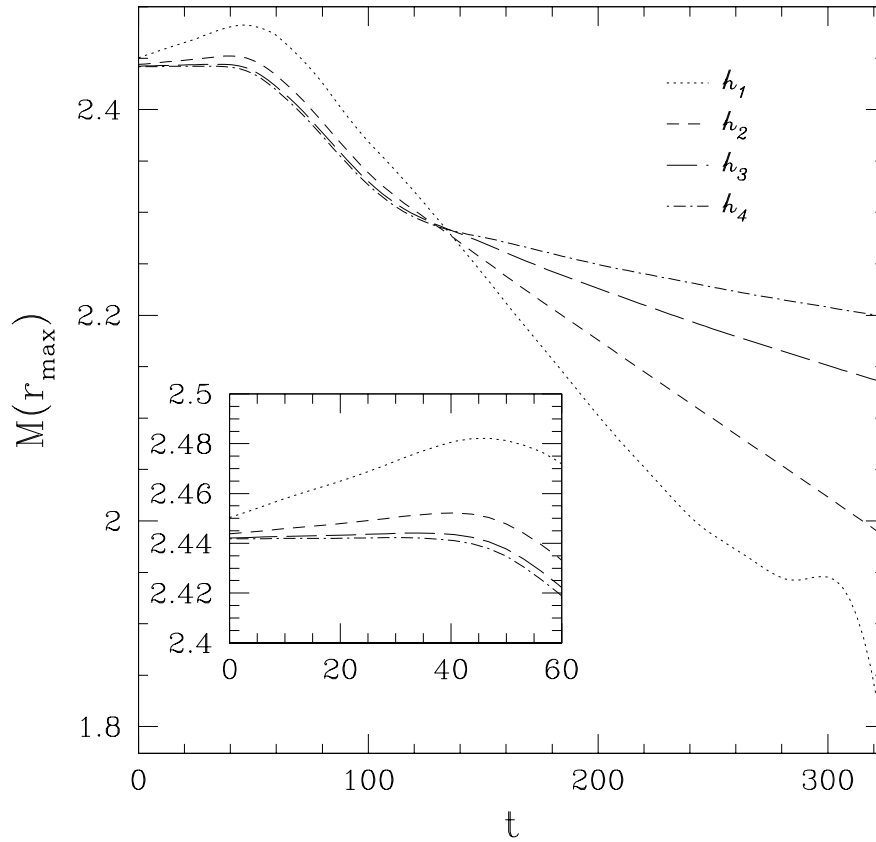
and show that it is conserved during the period in which all particles remain within the computational domain. Secondly, Fig. 4.4 displays the convergence

Figure 4.1: Sample convergence test (CT) of the stress energy component T_r^t at t=30.
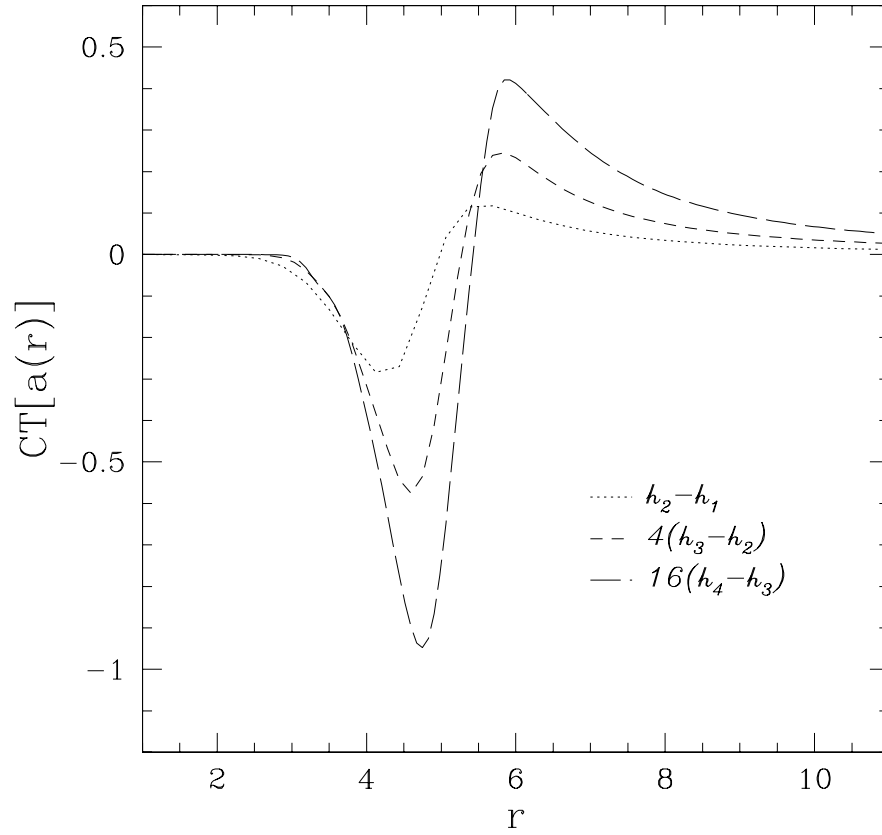
Figure 4.2: Sample convergence test (CT) of the metric function $a(t, r)$ at t=90.

Figure 4.3: .
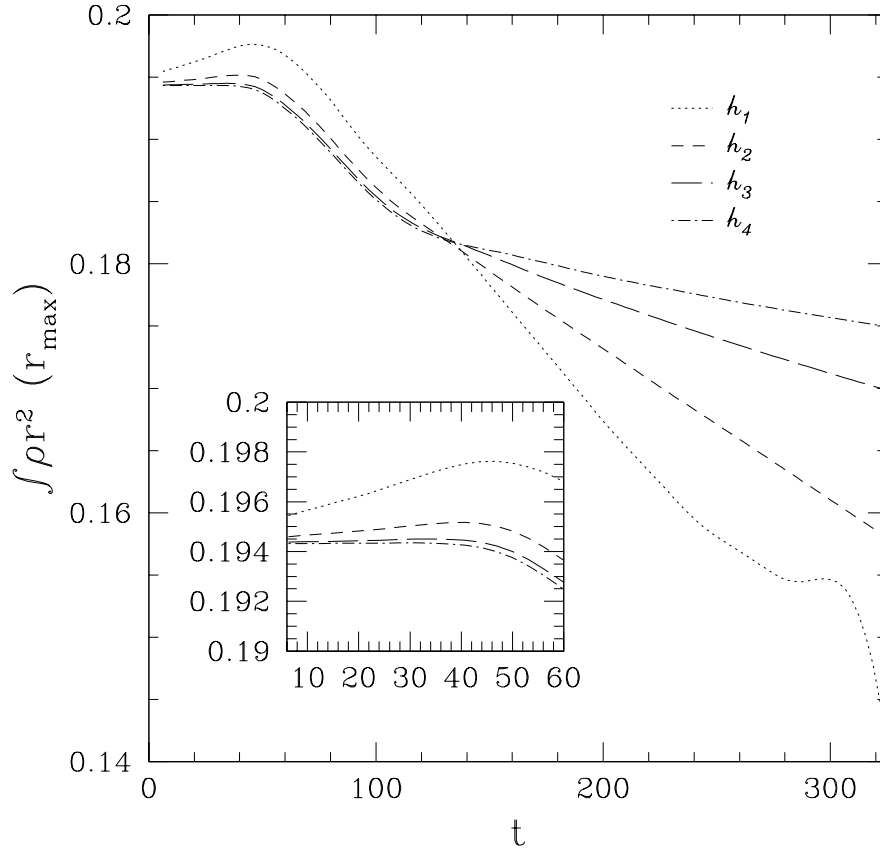Convergence of ADM mass conservation. Note that the pulse begins to leave the computational domain at around $t \approx 45$. At initial times, as shown in the inset, this plot indicates convergence to conservation of a mass ≈ 2.44. After the mass has been shed from $t \approx 45$ to $t \approx 130$, there appears to be linear conservation (in h) to a final mass ≈ 2.275.

of the mass as computed via integration of the energy-density ρ, or $-T_t^t$, to $r = r_{\max}$.

The strong evidence is that both measures of the mass are converging in the limit $h \to 0$.

Figure 4.4: Convergence of energy conservation. Note that the pulse begins to leave the domain at around $t \approx 45$. At initial times, as shown in the inset, this plot indicates convergence to conservation of an integrated energy ≈ 0.19425. After the mass has been shed from $t \approx 45$ to $t \approx 130$, there appears to be linear convergence (in h) to a continuum total integrated energy ≈ 0.1825.

CHAPTER 5

RESULTS FOR ONE VALUE OF L^2

We now move on to show evidence for the existence of a Type I (static) critical solution, and illustrate how the time derivatives of the metric variables apparently converge to zero with increasing resolution. Finally, we describe the expected and observed scaling behavior of the lifetimes of near-critical solutions, and tabulate the scaling parameters for various sets of initial data.

As described previously, we deal with distribution functions describing particles with fixed angular-momentum-squared, l^2. Specifically, our initial data is of the form

$$f(0, r, p_r, l^2) = A \, \exp\left(-\left(\frac{r - r_o}{\Delta_r}\right)^2\right) \exp\left(-\left(\frac{p_r - p_{r_o}}{\Delta_{p_r}}\right)^2\right) \delta(l^2 - l_o^2) \quad (5.1)$$

5.1 Static Critical Solutions

Type I critical solutions are conjectured to be either static or periodic. We now present evidence that the Einstein-Vlasov model studied here admits static Type I critical solutions. By way of a bisection search, we are able to tune one parameter to machine precision, 16 digits, in order to best approximate the critical solution (at fixed resolution). The fairly mundane recipe for conducting a bisection search is now described: Begin with a "bracket": one solution which evolves to form a black hole, called "high", and another solution which disperses, called "low". Let us say that "high" corresponds to a larger value of a parameter

Table 5.1: Scaling parameter σ for various initial conditions defining the distribution function in (5.1).

l^2	r_o	Δr	p_{r_o}	Δp_r	σ
400	5.0	1.0	0.0	2.0	-11.21
144	5.0	1.0	0.0	2.0	-11.09
64	5.0	1.0	0.0	2.0	-9.58
16	5.0	1.0	0.0	2.0	-5.27
144	5.0	2.0	0.0	1.0	-11.65
144	5.0	1.0	-1.0	2.0	-8.63

p in the initial data, and "low" to a smaller value of the same parameter; the total initial mass, for example. Now "tune" p to approximate the threshold between high solutions and low solutions by continually taking it as the average of the most recent high and low runs. Do this until machine precision is reached—typically 25-30 trials.

The above procedure was conducted for several sets of initial conditions. In each case, a near-static approximation to a critical solution that was nearly static was obtained. Note that although the distribution functions themselves are not stationary, the metric coefficients represent a static metric and their time derivatives converge to zero—showing strong evidence for staticity. As a typical example, Figure 5.1 shows the time derivative of the metric function $a(t, r)$ at a variety of different times during an evolution, at 4 different resolutions. The time derivative of $a(t, r)$ more closely approximates zero with increasing resolution. Similar behavior is exhibited for all initial data profiles, and we therefore conjecture the existence of a static critical solution.
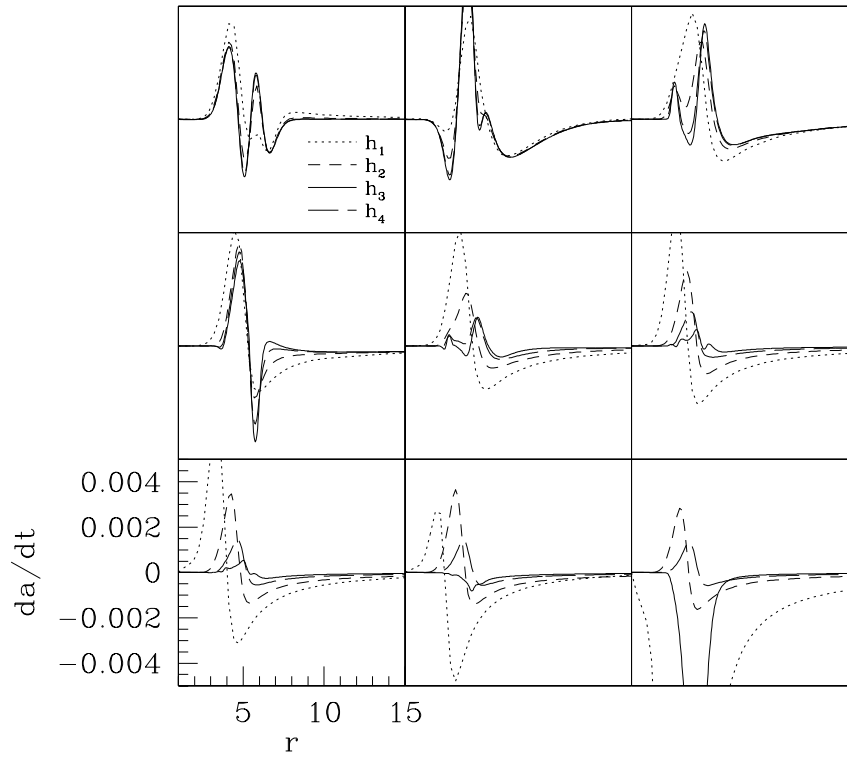
Figure 5.1: Convergence to zero of time derivative of metric coefficient $a(t, r)$. While this is not a convergence plot *per se*, since we have a different $p^\star$ at each resolution, it does show that as we increase resolution, the time derivative of $a(t, r)$ more closely indicates a static metric. Arguably, this is a *stronger* demonstration of convergence to a *static* solution in the continuum limit than a "traditional" convergence test (which would be done at fixed parameter value, p) would provide.

5.2 Scaling

Solutions in the vicinty of Type-I critical solutions (i.e. those solutions with $p \approx p^\star$) are known to have "lifetime scaling"" laws of the form

$$|t - t^\star| = \ln |p - p^\star|^\sigma \tag{5.2}$$

Here t represents the time a solution defined by parameter p is "near" the closest critical solution defined by $p^\star$, and $t^\star$ is some fiducial reference time. Indeed since scaling law (5.2) really relates the *change* in $|t - t^\star|$ to the change in $|p - p^\star|$, the definition of this "near-to-criticality" time is only defined up to an arbitrary constant.

In the inset of Figure 5.2 we show a typical scaling relationship of the form (5.2)—including an estimate of the scaling exponent, σ, that we are able to extract from our numerical results. It is apparent from the linear relationship between $|t - t^\star|$ and $\ln |p - p^\star|$ that the data does conform to (5.2), and we thus have ever stronger evidence that previously [19, 20] that the critical solutions in this model are *static*, and one-mode unstable [13].

As further evidence that the scaling relationship is indeed linear, we plot the difference between the best fit line obtained at the highest resolution and the scaling behavior obtained at successively coarser resolutions in Figure 5.2. We see that as resolution is increased, the residuals more closely approximate a straight line.

We tabulate scaling exponents for a variety of initial data in Table 5.1, and note that they are neither unique nor universal. Further work must be done in order to determine whether the scaling exponent is universal with respect to some specific dimensionless parameter.
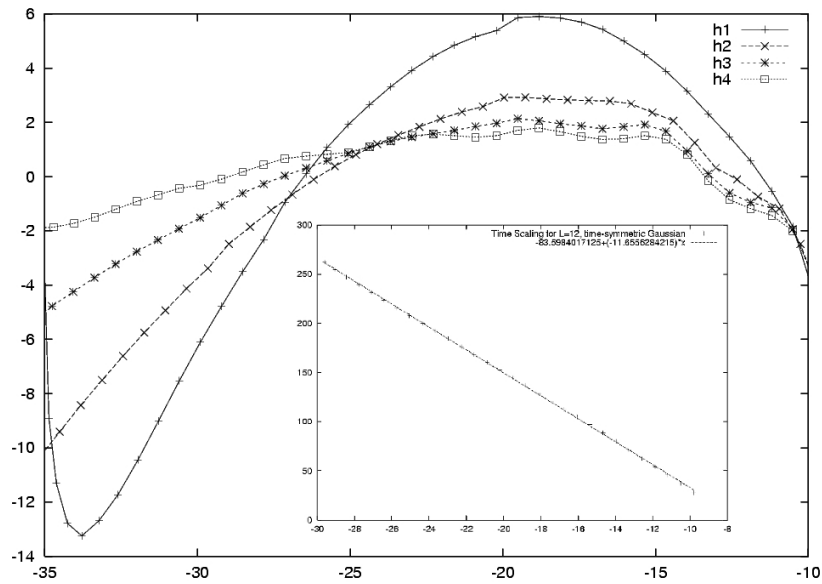
Figure 5.2: The best fit line at highest resolution, shown in inset, minus $(t-t^\star)$ at four different resolutions, plotted against $\ln|p-p^\star|$. Note that as resolution is increased the difference converges to zero above some $\ln|p-p^\star| \approx -15$ which we call the "critical regime". In the inset we have a demonstration that the relationship between $t-t^\star$ and $\ln|p-p^\star|$ is indeed linear. The slope is listed in Table 5.1.
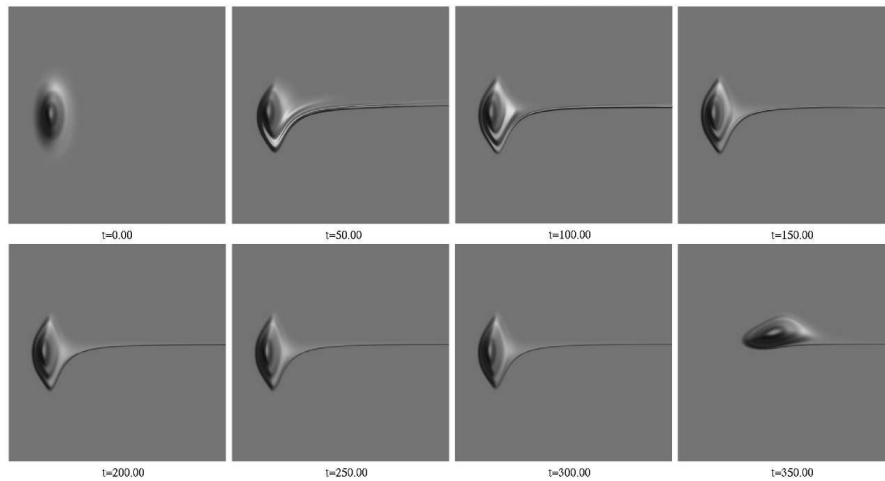
Figure 5.3: Time evolution of distribution function $f(t, r, p_r)$ for $l^2 = 12$ critical solution. Evolution proceeds left to right, top to bottom. In each frame the x-axis is radius, r, while the y-axis is radial momentum, p_r. Note that during the critical regime—roughly, frames 2 through 7—the distribution function is approximately symmetric with respect to the $p_r = 0$ axis, as must be the case for a static solution. This emphasizes the highly non-trivial and time-dependent radial behaviour of the particles in the critical solution. In contrast, for example, with the Einstein-cluster solutions to this model, which describe clusters of particles on purely circular orbits, the individual particles in the critical solution are constantly moving in and out radially, but in such a fashion that, collectively, the distribution function is static.

CHAPTER 6

RESULTS FOR TWO VALUES OF L^2

We now discuss the critical collapse of two distributions comprised of two species of particles with distinct values of the angular momentum parameter, l^2. We provide evidence for Type I (static) critical solutions, describe the expected scaling behavior of solutions, and tabulate the scaling parameters for various sets of initial data.

In this chapter our initial data is composed of a linear superposition of two distribution functions. Each distribution has particles with a particular value of angular-momentum-squared. Specifically, our initial data has the form:

$$
\begin{aligned}
f(t, r, p_r, l^2) &= A_1 \exp\left(-\left(\frac{r - r_1}{\Delta_{1r}}\right)^2 - \left(\frac{p_r - p_{r_1}}{\Delta_{1p_r}}\right)^2\right) \delta(l^2 - l_1^2) \quad (6.1) \\
&+ A_2 \exp\left(-\left(\frac{r - r_2}{\Delta_{2r}}\right)^2 - \left(\frac{p_r - p_{r_2}}{\Delta_{2p_r}}\right)^2\right) \delta(l^2 - l_2^2)
\end{aligned}
$$

We now outline the form of our bisection search method for two distribution functions of varying angular momenta, and then tabulate scaling parameters for a variety of initial conditions.

6.1 Bisection Search and Critical Behavior

The critical parameter p which forms the basis for our bisection search is the amplitude of the first distribution, A_1. By varying p we can form super- and

Table 6.1: Scaling parameter σ for various initial conditions defining the distribution function in (6.1)

l_1^2	r_1	Δr_1	p_{r1}	Δp_{r_1}	l_2^2	r_2	Δr_2	p_{r_2}	Δp_{r_2}	σ
144	12.0	1.0	-2.0	1.0	169	12.0	1.0	-2.0	1.0	-9.25
144	12.0	1.0	-2.0	1.0	169	12.0	1.0	-1.0	1.0	-9.83
144	12.0	1.0	-2.0	1.0	196	12.0	1.0	-1.0	1.0	-9.30
400	5.0	1.0	0.0	2.0	144	5.0	2.0	0.0	1.0	-11.65

sub-critical evolutions. For $p > p^\star$ we have a situation where both distribution functions collapse to form a black hole, and for $p < p^\star$ both disperse. Defining the critical regime as a particular radius that both distribution functions are within, we find that for $p \to p^\star$, the time both distributions are in the critical regime scales as expected:

$$|t - t^\star| = \ln |p - p^\star|^\sigma$$

The estimated scaling exponents, σ for a variety of initial conditions are tabulated in Table 6.1.

6.2 Convergence, Conservation, and Staticity

Convergence and conservation of mass and energy were tested in each of the solutions listed in Table 6.1, yielding results similar to those shown in Figures 4.4, 4.2, 4.1, and 4.3. Furthermore, an increasingly static metric was achieved as resolution increased, thus exhibiting behavior similar to that shown in Figure 5.1.

CHAPTER 7

RESULTS FOR MASSLESS CASE

In [13] it was proposed that the massless Einstein-Vlasov case should not exhibit Type I critical phenomena. We now present evidence to the contrary: such a system *does* seem to exhibit the staticity and lifetime-scaling associated with Type I critical phenomena.

Specifically, in both one- and two-distribution function calculations at one and two angular momenta respectively, Type I scaling and staticity are both manifest.

The scaling parameters for a variety of initial conditions are given in Table 7.1.

Table 7.1: Scaling parameter σ for various initial conditions defining the massless distributions according to (6.1).

l_1^2	r_1	Δr_1	p_{r1}	Δp_{r_1}	l_2^2	r_2	Δr_2	p_{r_2}	Δp_{r_2}	σ
144	12.0	1.0	-2.0	1.0	169	12.0	1.0	-2.0	1.0	-9.13
144	12.0	1.0	-2.0	1.0	196	12.0	1.0	-2.0	1.0	-9.51

CHAPTER 8

CONCLUSIONS AND DISCUSSION

Our studies of the spherically-symmetric Einstein-Vlasov system provide strong evidence for the existence of Type I critical solutions. Within the context of our ansatz, in which all particles have the same angular momentum, all near-critical solutions approach static spacetimes and the lifetimes of near-critical solutions satisfy scaling laws as expected. We have also show that similar behaviour is seen for the case of two-species calculations, where the l^2 for each species is constant. Finally, and contrary to some expectations discussed in the literature, we have found strong evidence that the black hole transition in this model remains Type I, with static critical solutions, even in the limit of massless particles.

The focus of futher work should be in determining whether or not the critical solution is universal, up to an arbitrary rescaling of space and time variables. This has not been determined in this thesis, and will require one to deduce the dimensionless variables that govern the rescaling.

Another future avenue is to look at the logarithmic scaling of angular momentum to see whether the critical solution persists across a large range of angular momenta. In calculations, the distribution function, f, becomes increasingly prolate or oblate, depending on the ratio of radial kinetic energy to angular momentum. Resolving very prolate or very oblate configurations requires large computational domains and computation times that are beyond our current means.

Notably however, what this thesis *does* provide is a demonstrably convergent

implementation of a finite volume method that solves the spherically symmetric Einstein-Vlasov system. This method is not subject to the statistical fluctuations seen in earlier Monte-Carlo-based work, but rather has "good" convergence properties as one expects for finite volume approximations of smooth solutions ot partial differential equations. This well defined and regular convergence behaviour is crucial in providing convincing evidence that the Type I critical behaviour seen in this model is characterized by *static* solutions.

BIBLIOGRAPHY

[1] Dafermos M & Rendall AD, "An Extension Principle for the Einstein-Vlasov System in Spherical Symmetry", gr-qc/0411075 (2004)

[2] Tchapnda SP & Rendall AD, "Global Existence and Asymptotic Behaviour in the Future for the Einstein-Vlasov System with Positive Cosmological Constant", *Class Quant Grav*, **20**, 3037–3049 (2003)

[3] Coleman JS & Evans CR, "Critical Phenomena and Self-Similarity in the Gravitational Collapse of Radiation Fluid", *Phys Rev Lett*, **72**, 1782–1785 (1994)

[4] Choptuik MW, "Universality and Scaling in the Gravitational Collapse of a Scalar Field", *Phys Rev Lett*, **70**, 9–12 (1993) *Phys Rev Lett*, **70**

[5] Choptuik MW, "The 3+1 Einstein Equations"
http://laplace.physics.ubc.ca/T/98Spring/Phy387N/Doc/3+1.ps
Unpublished notes (1998)

[6] Choptuik MW, 'Finite Difference Methods"
http://laplace.physics.ubc.ca/T/00Fall/PHYS410/Doc/fd/ex1/lecture.ps
Unpublished notes (2002)

[7] Choptuik MW, Personal communication (2005)

[8] Choptuik MW, Personal communication (2005)

[9] Christodoulou D, "A Mathematical Theory of Gravitational Collapse", *Commun Math Phys*, **109**, 613–647, (1987)

[10] Christodoulou D, "The Formation of Black Holes and Singularities in Spherically Symmetric Gravitational Collapse", *Commun Pure Appl Math*, **44**, 339–373, (1991)

[11] Neilsen DW & Choptuik MW, "Critical Phenomena in Perfect Fluids", *Class Quant Grav*, **17**, 761–782, (2000)

[12] Schaeffer J, Rein G and Rendall AD, "Critical Collapse of Collisionless Matter: A Numerical Investigation", *Phys Rev*, **D58**:044007 (1998)

[13] Gundlach C & Martin-Garcia JM, "Self-similar Spherically Symmetric Solutions of the Massless Einstein-Vlasov System", *Phys Rev*, **D65**:084026, (2002)

[14] Gundlach C, "Critical Phenomena in Gravitational Collapse", *Phys Rept*, **376**, 339–405, (2003)

[15] Leveque RJ, *Finite Volume Methods for Hyperbolic Problems*, Cambridge University Press, Cambridge UK, (2002)

[16] Choptuik MW, Chmaj T & Bizon P, "Critical Behavior in Gravitational Collapse of a Yang-Mills Field", *Phys Rev Lett*, **77** 424–427, (1996)

[17] Choptuik MW, Liebling SL, Hirschmann EW & Pretorius F, "Critical Collapse of a Massless Scalar Field in Axisymmetry", *Phys Rev*, **D68**:044007, (2003)

[18] Choptuik MW, Liebling SL, Hirschmann EW & Pretorius F, "Critical Collapse of a Complex Scalar Field with Angular Momentum", *Phys Rev Lett*, **93**:131101 (2004)

[19] Olabarrieta, I, *Critical Collapse of Collisionless Matter in Spherical Symmetry*, UBC MSc Thesis, (2000)

[20] Olabarrieta I & Choptuik, MW, "Critical Phenomena at the Threshold of Black Hole Formation for Collisionless Matter in Spherical Symmetry", *Phys Rev*, **D65**:024007, (2002)

[21] Brady PR, Choptuik MW. Gundlach C, Neilsen DW, "Black Hole Threshold Solutions in Stiff Fluid Collapse", *Class Quant Grav*, **19**, 6359–6375, (2002)

[22] Rendall AD, "An Introduction to the Einstein-Vlasov System", gr-qc/9604001 (1996)

[23] Liebling SL, Hirschmann EW & Isenberg J, "Critical Phenomena in Nonlinear Sigma Models", *J Math Phys*, **41**, 5691–5700, (2000)

[24] Teukolsky SA & Shapiro SL, "Relativistic Stellar Dynamics on the Computer I: Motivation and Numerical Method", *Ap J*, **298**, 34–57, (1985) Teukolsky SA & Shapiro SL, "Relativistic Stellar Dynamics on the Computer II: Applications", *Ap J*, **298**, 58–79, (1985) Teukolsky SA & Shapiro SL, "Relativistic Stellar Dynamics on the computer IV: Collapse of a Star Cluster to a Black Hole", *Ap J*, **307**, 41–44, (1985)

[25] York JW Jr, "Kinematics and Dynamics of General Relativity" in *Sources of Gravitational Radiation: Proceedings of the Battelle Seattle Workshop*, Smarr L, ed, Cambridge University Press, Cambridge UK, (1979)

APPENDIX A

CHRISTOFFEL SYMBOLS FOR POLAR-AREAL METRIC

The polar-areal line element used in the body of the thesis is

$$ds^2 = -\alpha^2(t,r)dt^2 + a^2(t,r)dr^2 + r^2 d\Omega^2$$

Straightforward comoputations of the Christoffel symbols, $\Gamma^c{}_{ab}$, using

$$\Gamma^c{}_{ab} = \frac{1}{2}g^{cd}\left(\partial_a g_{bd} + \partial_b g_{ad} - \partial_d g_{ab}\right)$$

then yields the following non-trivial components.

$$
\begin{aligned}
\Gamma^r{}_{rr} &= \frac{a'}{a} & \Gamma^r{}_{\theta\theta} &= -\frac{2r}{2a^2} & \Gamma^r{}_{\phi\phi} &= -\sin^2\theta\frac{2r}{2a^2} \\
\Gamma^\theta{}_{r\theta} &= \frac{2r}{2r^2} & \Gamma^\theta{}_{\phi\phi} &= -\sin\theta\cos\theta \\
\Gamma^\phi{}_{r\phi} &= \frac{2r}{2r^2} & \Gamma^\phi{}_{\theta\phi} &= \cot\theta
\end{aligned}
\tag{A.1}
$$